

The Megamaser Cosmology Project: IV.

A Direct Measurement of the Hubble Constant from UGC 3789

M. J. Reid¹, J. A. Braatz², J. J. Condon², K. Y. Lo², C. Y. Kuo², C. M. V. Impellizzeri² & C. Henkel^{3,4}

ABSTRACT

In Papers I and II from the Megamaser Cosmology Project, we reported initial observations of H₂O masers in an accretion disk of a supermassive black hole at the center of the galaxy UGC 3789, which gave an angular-diameter distance to the galaxy and an estimate of H_0 with 16% uncertainty. We have since conducted more VLBI observations of the spatial-velocity structure of these H₂O masers, as well as continued monitoring of its spectrum to better measure maser accelerations. These more extensive observations, combined with improved modeling of the masers in the accretion disk of the central supermassive black hole, confirm our previous results, but with significantly improved accuracy. We find $H_0 = 68.9 \pm 7.1 \text{ km s}^{-1} \text{ Mpc}^{-1}$; this estimate of H_0 is independent of other methods and is accurate to $\pm 10\%$, including sources of systematic error. This places UGC 3789 at an angular-diameter distance of $49.6 \pm 5.1 \text{ Mpc}$, with a central supermassive black hole of $(1.16 \pm 0.12) \times 10^7 M_\odot$.

Subject headings: Hubble Constant — Cosmology — Dark Energy — General Relativity — distances — individual sources (UGC 3789)

1. Introduction

Measurements of the expansion history of the universe, $H(z)$, play a fundamental role in our understanding of cosmological evolution and its far-reaching physical implications, including addressing the nature of dark energy, the curvature of space, the masses of neutrinos, and the number of families of relativistic particles. While detailed measurements of the

¹Harvard-Smithsonian Center for Astrophysics, 60 Garden Street, Cambridge, MA 02138, USA

²National Radio Astronomy Observatory, 520 Edgemont Road, Charlottesville, VA 22903

³Max-Planck-Institut für Radioastronomie, Auf dem Hügel 69, 53121 Bonn, Germany

⁴King Abdulaziz University, P.O. Box 80203, Jeddah, Saudi Arabia

cosmic microwave background (CMB, e.g. Komatsu et al. (2011)) allow us to measure linear scales at redshift $z \approx 1100$, this mostly provides information at a single epoch and when the influence of dark energy was still negligible. Complementary information from later cosmic times are therefore essential. This information can come from type Ia supernovae, galaxy clustering, gravitational lensing, and baryon acoustic oscillations (e.g. Riess et al. (2011); Bonamente et al. (2006); Suyu et al. (2010); Reid et al. (2010)).

All of these data provide distances and linear scales at significant redshifts. However, it is the local universe where dark energy is dominant. Thus the local Hubble constant, H_0 , provides the largest “lever arm” with respect to the CMB for constraining the time dependence of the equation of state of dark energy. The use of Cepheids (e.g. Freedman et al. (2001); Sandage et al. (2006)) as well as the combined use of Cepheids and Type Ia supernovae (e.g. Riess et al. (2011)) has traditionally dominated determinations of H_0 . What is missing, however, are direct geometric distance estimates that do not require a complex and uncertain ladder of calibration of “standard candles.”

Direct geometric distance measurements to water masers in nuclear regions of galaxies that are well into the Hubble flow (roughly > 30 Mpc distant) provide a promising new and independent method for refining the value of H_0 . Observations of water masers in accretion disks within ~ 0.1 pc of a galaxy’s central supermassive black hole have been used to measure angular-diameter distances to galaxies, independently of other techniques that often rely on standard candles. Very Long Baseline Array (VLBA) observations of the H_2O masers in the nearby Seyfert 2 galaxy NGC 4258 established the technique and provided an accurate, angular-diameter distance of 7.2 ± 0.5 Mpc to the galaxy (Herrnstein et al. 1999). This galaxy is too close to permit a direct measurement of H_0 (i.e. by dividing its recessional speed by its distance), since its uncertain peculiar velocity could be a large fraction of its recessional speed. However, NGC 4258 has proven extremely valuable as a solid anchor for the extragalactic distance scale (Freedman et al. 2001; Riess et al. 2011).

Recently, the Megamaser Cosmology Project (MCP) reported a distance to UGC 3789, another galaxy with water masers in a nuclear accretion disk, of 49.9 ± 7.0 Mpc (Reid et al. 2009; Braatz et al. 2010) (hereafter Papers I and II). This galaxy has a recessional velocity of $\approx 3481 \text{ km s}^{-1}$ (relativistically corrected and referenced to the cosmic microwave background), which includes its peculiar velocity of $151 \pm 163 \text{ km s}^{-1}$ based on galaxy flow models of Masters et al. (2006) and Springob et al. (2007)). Combining the recessional velocity and distance yielded $H_0 = 69 \pm 11 \text{ km s}^{-1} \text{ Mpc}^{-1}$.

Since UGC 3789 is well into the Hubble flow it can provide a direct estimate of H_0 with a potential uncertainty as small as $\pm 5\%$, limited by the uncertainty in its peculiar motion. Therefore, since reporting our initial results, we have conducted additional observations of

UGC 3789, in order to reduce the uncertainty of the H_0 estimate. In total, we have now analyzed nine Very Long Baseline Interferometric (VLBI) observations, using the NRAO ¹ 10-antenna VLBA, the 100-m Green Bank Telescope (GBT) and the 100-m Effelsberg ² telescope. The VLBI observations are reported in §2. We have also extended our monitoring of changes in the water maser spectrum with monthly observations (except during the humid summer) with the GBT for a period spanning 5.5 years. These spectra are documented in §3 and used to determine the accelerations of individual maser features. In §4, we describe a Bayesian approach for fitting a model of the accretion disk to these data. The model allows for a warped disk with eccentric gas orbits and includes parameters for the central (black hole) mass and position, as well as for H_0 .

2. VLBI Imaging

VLBI observations were conducted at nine epochs (NRAO program codes BB227A, BB227B, BB242A, BB242I, BB242K, BB242L, BB242Q, BB261G, and BB261S) between December 2007 and April 2010. Six of the nine observations yielded maps with signal-to-noise ratios degraded by factors of two or greater owing to the loss of one of the 100-m telescopes (usually to poor weather) or the weakening of the peak maser emission to levels where self-calibration (phase-referencing) using the maser emission was poor. The three epochs with excellent weather, antenna performance, and strong maser emission included BB227A (2006 December 10; reported in Paper I), BB242L (2008 December 12), and BB261G (2009 April 11). Only results from these three epochs are reported here.

We observed with 16-MHz bands covering five frequencies, three in dual polarization and two in single polarization. In our early observations, these bands were centered at (optical definition) local standard of rest (LSR) velocities (and polarizations) of 3880.0 (LCP & RCP), 3710.0 (LCP), 3265.0 (LCP & RCP), 2670.0 (LCP & RCP), and 2500.0 (LCP) km s^{-1} for BB227A; for the BB242L and BB261G, we shifted the center velocities of the fourth and fifth bands to 2717.6 and 2513.6 km s^{-1} , in order to map new maser features not covered in the original setup. The data for each polarization of each band were cross-correlated with 128 spectral channels, yielding channels separated by 1.7 km s^{-1} .

Generally, the data were analyzed as described in Paper I. The final calibration step involved selecting a maser feature as the interferometer phase-reference, and details of this

¹The National Radio Astronomy Observatory is operated by Associated Universities, Inc., under a cooperative agreement with the National Science Foundation.

²The Effelsberg 100-m telescope is a facility of the Max-Planck-Institut für Radioastronomie

procedure varied among epochs depending on maser strength and interferometer coherence times. The strongest maser feature in the spectrum usually peaked at ≈ 0.07 Jy and was fairly broad. For BB227A, we averaged five spectral channels spanning an LSR velocity range of 2685 to 2692 km s⁻¹ (i.e. channels 52 to 56 from the blue-shifted high-velocity band centered at $V_{\text{LSR}} = 2670$ km s⁻¹), adding together the data from both polarizations, and fitting fringes over a 1 min period. For BB242L, we averaged 13 spectral channels spanning an LSR velocity range of 2682 to 2702 km s⁻¹ (i.e. channels 74 to 86 from the blue-shifted high velocity band centered at $V_{\text{LSR}} = 2717.6$ km s⁻¹) and fitted fringes over a 2 min period. For BB261G, we averaged seven spectral channels spanning an LSR velocity range of 2685 to 2696 km s⁻¹ (i.e. channels 78 to 84 from the blue-shifted high velocity band centered at $V_{\text{LSR}} = 2717.6$ km s⁻¹), again with 2 min averaging.

After calibration, we Fourier transformed the gridded (u,v) -data to make images of the maser emission in all spectral channels for each of the five IF bands. The images were deconvolved with the point-source response using the CLEAN algorithm and restored with a circular Gaussian beam with a 0.30 mas full-width at half-maximum (approximately matching the geometric mean of the dirty beam). The rms noise levels in channel maps were ≈ 1 mJy. All images appeared to contain single, point-like maser spots. We then fitted each spectral-channel image with an elliptical Gaussian brightness distribution in order to obtain positions and flux densities.

Spectral images for the three epochs are shown in Fig. 1 for maser spots stronger than 5 mJy. (Note, that in Paper I, we displayed only maser spots stronger than 10 mJy.) These images show nearly identical spatial-velocity patterns of maser emission. This is expected as material in near-circular orbit in the accretion disk at the average masing radius has an orbital period of ~ 1000 yr and thus rotates by less than 1° of disk azimuth between the first and last observation. Most of the spatial scatter in the images is from measurement uncertainty, primarily from signal-to-noise limitations, of $\approx 25 \mu\text{as}$ for weaker features of ≈ 10 mJy.

3. GBT Spectral Monitoring and Acceleration Fitting

Paper II describes the procedures used to monitor the H₂O maser spectrum of UGC 3789 from January 2006 to March 2009 with the GBT. We continued these observations through June 2011. Typically, observations were conducted at monthly intervals for nine months per year, avoiding the summer when atmospheric water vapor precluded sensitive observations. These spectra were divided into 6 yearly blocks and analyzed to determine velocity drifts (accelerations) of individual maser features.

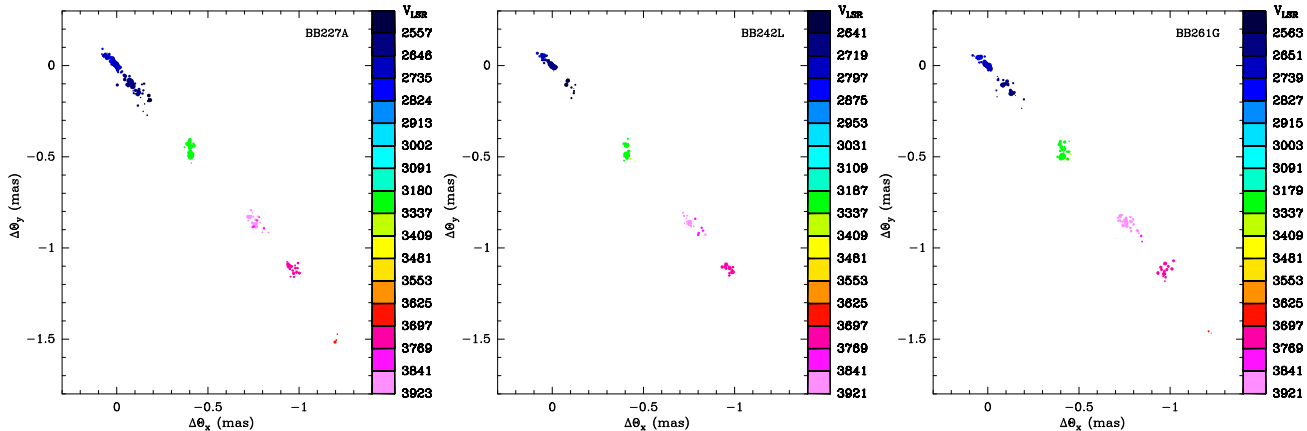


Fig. 1.— Maps of the 22 GHz H_2O masers toward UGC 3789 constructed from VLBI data using the VLBA, the GBT and the Effelsberg antennas for programs BB227A (2006 December 10), BB242L (2008 December 12) and BB261G (2009 April 11). The LSR velocity of each maser spot is indicated by the color bar on the right side of each panel.

Measurement of the acceleration of systemic-velocity masers is key to determining the angular-diameter distance of the galaxy. In principle, accelerations are straight-forwardly obtained from the linear drift in peak velocity with time. In practice, however, blending of adjacent spectral features, coupled with modest signal-to-noise ratio observations, makes this difficult. We applied two methods described below to measure accelerations: method-1 to obtain the best acceleration estimates and method-2 to check for possible fitting biases owing to initial parameter values.

3.1. Method–1

In Paper II we measured accelerations in two steps. First, we identified spectral peaks in individual spectra “by eye” and tracked these peak velocities over time to obtain preliminary accelerations. Then, we modeled the spectral flux density as a function of velocity and time as the sum of a number of Gaussian spectral lines, whose center velocity changes linearly with time. We repeated this approach with the extended spectral monitoring data.

Parameters for individual Gaussian components included the amplitudes (one per observational epoch), the line width, and the center velocity (at a reference epoch) and its (linear) change in velocity over time. Initial values for maser component velocities and accelerations were set based on the “by eye” values; line widths were initially set at 2.0 km s^{-1} and assumed not to vary over the ≈ 9 months of observations being analyzed. Initial values for

maser component amplitudes for each observation were set automatically at the flux density of each spectrum at the velocity determined by the initial central velocity and acceleration parameters.

The parameters were adjusted by a sequence of least-square fitting (to minimize the sum of the squares of the weighted post-fit residuals or χ^2). In the first fitting step, only the amplitudes were adjusted. Next, the amplitudes, central velocities and line widths were adjusted, using parameter values derived from the first fits. Finally, all parameters (including accelerations) were allowed to vary. While this least-squares approach works well and gives accelerations that largely agree with those visually evident in the spectra, it is a time-consuming process and dependent on somewhat subjectively determined initial parameters.

3.2. Method–2

In order to avoid setting the initial velocities and acceleration parameters by eye, we developed an alternative analysis method. This method involved randomly choosing initial values followed by least-squares fitting and evaluation of the quality of each fit. We repeated this process, with independently chosen initial parameter values, about 100 times and recorded the four fits with the lowest values of χ^2 per degree of freedom. In detail, for each trial solution, we assigned the center velocity, V_n , of the n^{th} spectral component by selecting a velocity offset randomly, from a Gaussian distribution with a mean of 2.0 km s^{-1} and a standard deviation of 0.7 km s^{-1} , and adding this offset to the central velocity of the $(n-1)^{\text{th}}$ component. We started at the low end of the velocity “window” being fitted and continued until we reached the high end; this allowed different trial fits to have different numbers of velocity components.

Since the change in component acceleration with velocity is generally small, rather than set accelerations independently for each component as in method–1, we set a single acceleration and its velocity derivative (2 parameters) for the entire velocity window under consideration. This minimizes the number of free parameters, but requires setting small velocity windows over which component accelerations are nearly constant. Specifically, we assigned an initial acceleration, A_n , to the n^{th} velocity component given by $A_n = A_c + (dA/dV)(V_n - V_c)$, where V_c is the center of the velocity window, A_c is the average acceleration over the fitting window and dA/dV allows for a linear change in acceleration with velocity. Values of A_c were chosen randomly from a Gaussian distribution, whose mean was estimated from the fits described in method–1 and whose standard deviation, σ_A , was one-third of that mean. Values of dA/dV were chosen in a similar random manner from a distribution with zero mean and standard deviation of $\sigma_A/1 \text{ yr}$. The combined effect of the large standard

deviation for accelerations and allowance for a linear change in acceleration with velocity resulted in broad sampling of initial acceleration parameter space.

3.3. Acceleration Fitting Results

For systemic velocity features, we used three velocity windows for acceleration fitting: 3230–3280, 3286–3316, and 3350–3370 km s^{-1} , since emission outside of these windows was generally absent or very weak ($< 5 \text{ mJy}$). Systemic velocity maser features in UGC 3789 typically have lifetimes (with flux densities $> 5 \text{ mJy}$) of ~ 12 months. Therefore, we fitted accelerations separately to groups of ≈ 9 consecutive monthly spectra (from fall through spring) covering 5.5 years and centered at ≈ 2008.8 . These observations well-covered the three high-quality VLBI imaging observations discussed in this paper, whose mean epoch was ≈ 2008.4 .

Yearly acceleration measurements generally were consistent with a single value, although for some velocity ranges there was considerable scatter (up to about $\pm 30\%$ for masers near 3290 km s^{-1}). Because of this, and the expectation of small changes in acceleration over our observing period (as masing clouds move by less than 1° of disk azimuth), we velocity binned and averaged the fitted accelerations from the 6 “yearly” groups of spectra. Variance weighted averages of acceleration as a function of velocity for the systemic features are plotted Fig. 2 for both fitting methods outlined above.

The results for method-1 are plotted with filled (red) circles in Fig. 2. There is moderate scatter among the accelerations within each velocity window, and this scatter greatly exceeds that expected from the formal acceleration uncertainties. The greatest variations occur in the velocity range $3279 - 3330 \text{ km s}^{-1}$; we can bound this variation by assuming a constant acceleration over this velocity range and calculating a standard deviation of $1.6 \text{ km s}^{-1} \text{ yr}^{-1}$. We suspect that some of the variation is real and intrinsic to the source, but also that some of the variations may originate in the fitting process, owing to multiple velocity-blended components and using data with only moderate signal-to-noise ratios.

In order to provide an independent check on the results from method-1, we re-fitted the spectra using method-2. For each velocity window and each “yearly” time group, we selected the four trial fits with the lowest χ^2 values. We then binned all results in 2 km s^{-1} bins and calculated a weighted average acceleration for each velocity bin. These results are plotted in Fig. 2 with open (blue) squares. There is very good agreement between the two methods; the differences in average accelerations in each velocity window are small; unweighted means for methods-1 and -2 are 1.7 and $1.7 (\pm 0.2) \text{ km s}^{-1} \text{ yr}^{-1}$ for the velocity range 3230–3278

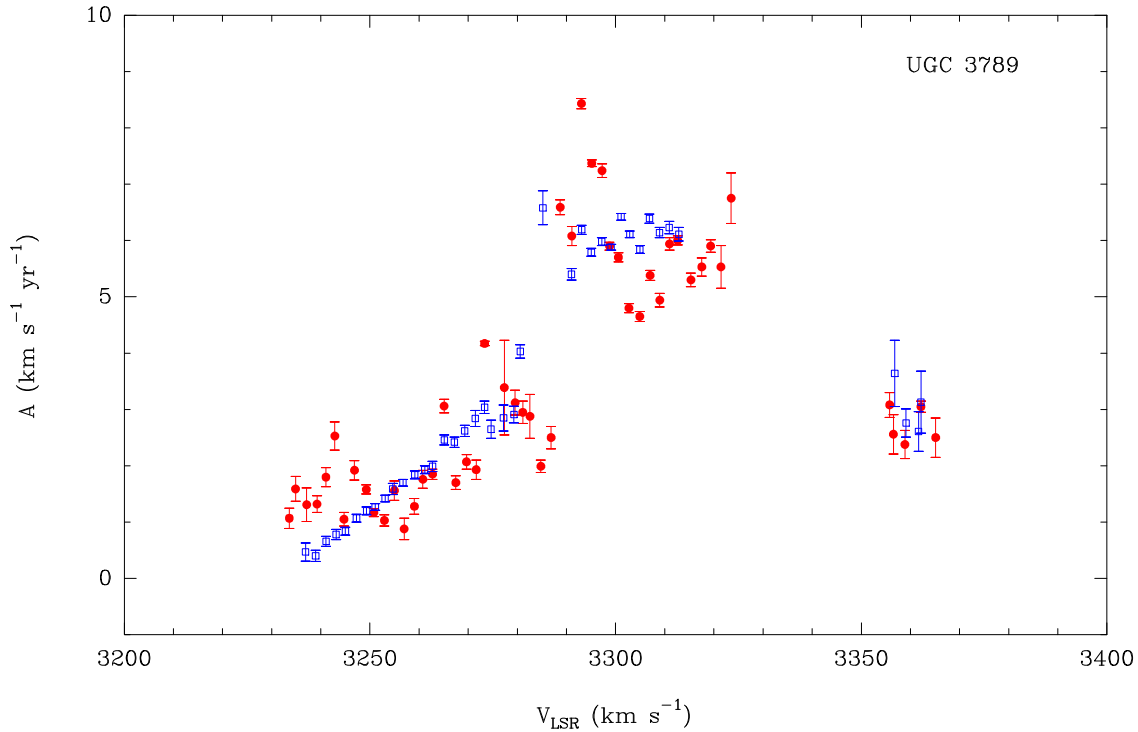


Fig. 2.— Acceleration measurements as a function of LSR velocity for systemic velocity maser features. *Filled red circles* are results from method-1 (see §3.1) and *open blue squares* are from method-2 (see §3.2).

km s^{-1} , 5.3 and $5.9 (\pm 0.4) \text{ km s}^{-1} \text{ yr}^{-1}$ for the velocity range $3279\text{--}3330 \text{ km s}^{-1}$, and 2.7 and $3.0 (\pm 0.3) \text{ km s}^{-1} \text{ yr}^{-1}$ for the velocity range $3350\text{--}3370 \text{ km s}^{-1}$. The small differences between the slopes of A vs. V_{LSR} for the two methods are within statistical uncertainties after accounting for the high correlation among accelerations within a window for method-2. We conclude that the accelerations given by the solid (red) points in Fig. 2 are near optimum values and are not significantly biased by the choice of initial parameter values in the first step of method-1.

Acceleration measurements for high velocity features are considerably less complicated as these features are not highly blended and have small changes in velocity over time. Therefore, we only used method-1 (described in §3.1) for these features, and fitted accelerations are given in Table 1.

4. Modeling the Accretion Disk & Estimating H_0

The position-velocity measurements from the three VLBI maps were combined by binning the velocities in 2.0 km s^{-1} wide bins (comparable to maser linewidths) and calculating

variance weighted positions and velocities. We associated these positions and velocities with maser feature accelerations, from the GBT time monitoring of spectra, by choosing the VLBI velocity closest to that of an acceleration fit. As there are fewer acceleration fits than VLBI position-velocity measurements, not all VLBI measurements have corresponding accelerations. For features lacking acceleration measurements we use only the position-velocity data when modeling. The velocity, position and acceleration values (when available) are given in Table 1 and used to model the accretion disk.

Rather than use formal fitting uncertainties, which tend to be optimistic for high signal-to-noise data, we adopted more realistic “error floors” for the data uncertainties of ± 0.01 mas for positions, ± 1.0 and ± 0.3 km s⁻¹ for the velocities of systemic and high-velocity maser features, respectively, and ± 0.57 km s⁻¹ yr⁻¹ for accelerations. Error floors were added in quadrature to formal fitting uncertainties. For example, systematic errors of ≈ 0.01 mas between systemic and high velocity features can be caused by an error in the absolute position of the reference maser spot of a few mas (Argon et al. 2007). Using error floors allows not only for systematic uncertainty not captured by formal estimates, but also for slight incompleteness in the model of the accretion disk, such as could come from unmodeled spiral structure. For example, there are indications of slight departures from perfect Keplerian gas orbits about a dominant central mass in the nearby, well-studied, disk of NGC 4258 at levels of ≈ 0.5 km s⁻¹ yr⁻¹ for systemic feature accelerations (Humphreys et al. 2008). In §4.1, we explore the sensitivity of the fitted parameters to changes in the magnitudes of these error floors.

Conceptually, were the masers in a perfectly thin and flat accretion disk orbiting circularly about a point mass and viewed edge-on, the position-velocity data for the high velocity features would trace a Keplerian profile (i.e. $V = \sqrt{GM/r}$), where G is the gravitational constant, M is the mass of the central black hole, and r is the distance of a masing cloud from the black hole. The symmetry of the approaching and receding features can be used to precisely locate the central black hole both in position (x_0, y_0) and velocity (V_0) . Thus, for high velocity features that are in the plane of the sky, the VLBI image directly gives a feature’s angular radius, $\theta = r/D$, where D is the distance to the galaxy. Systemic velocity masers in front of the black hole, moving transversely on the sky, display a change in velocity over time (A) as they orbit the central mass. Features in a thin annulus at radius, r , will be observed to accelerate at $A = V^2/r$. Thus, from position-velocity and acceleration measurements, one can estimate $D = V^2/A\theta$ and then $H_0 \approx V_r/D$, where V_r is the recessional velocity. Note that proper motions of systemic-velocity masers can also be used to estimate distance, and Herrnstein et al. (1999) showed that the proper motion distance agreed with the acceleration distance estimate for the nearby galaxy NGC 4258. However, proper motions decrease in magnitude with source distance and are generally far less ac-

curate than radial acceleration measurements based on changing Doppler shifts (which are distance independent).

In practice, accretion disks are somewhat more complicated than the idealized case just described. The disks are not precisely edge-on (although strong maser amplification prefers disk spin axes to be within about 5° of the plane of the sky (e.g. Watson & Wallin (1994)), disks are often somewhat warped, and gas may be on slightly eccentric orbits. Also, galaxies typically have peculiar motions of hundreds of km s^{-1} with respect to a pure Hubble flow (e.g. Masters et al. (2006)). These complications are best addressed by constructing a model for maser orbits in the disk and adjusting the model parameters to best match the observations.

We modeled the system with up to 13 global parameters. The central black hole has a mass, M , is located at (x_0, y_0) on the sky (relative to the reference maser feature) and has a line-of-sight velocity, V_0 , in the CMB rest frame. For UGC 3789, $V_0 = V_{\text{LSR}} + 60 \text{ km s}^{-1}$. Following Herrnstein et al. (1999), we model the disk warp by a change in inclination with radius, $i(r) = i_0 + (\partial i / \partial r) \delta r$, and position angle (defined east of north) with radius, $p(r) = p_0 + (\partial p / \partial r) \delta r$, where $\delta r = r - r_{\text{ref}}$ and r_{ref} is a reference radius assigned to the middle of the maser distribution. (Given the very small warping evident in the VLBI maps, we did not use second-order warping terms.) Our model can allow the masers to have eccentric orbits, with eccentricity e and pericenter rotated in angle $\omega = \omega_0 + (\partial \omega / \partial r) \delta r$ with respect to our line of sight. Finally, the galaxy (angular diameter) distance is calculated from H_0 , assuming its observed radial motion deviates from a pure Hubble flow by a peculiar velocity V_p relative to the cosmic microwave background reference frame. The angular diameter distance is calculated rigorously from formulae of Hogg (1999), assuming cosmological parameters for matter density $\Omega_m = 0.27$ and dark energy $\Omega_\Lambda = 0.73$.

We chose to estimate H_0 directly, rather than fit first for D , followed by a second step to estimate H_0 . There are several advantages in our approach. Firstly, unlike NGC 4258, which is not sufficiently distant to be in the Hubble flow and hence cannot be used to accurately estimate H_0 , for UGC 3789 our primary interest is H_0 and not D . Secondly, when solving for D , systemic feature accelerations, which are the least accurately measured type of data, appear in the denominator ($D = V^2 / A\theta$) and lead to an asymmetric posterior probability density function (PDF) and complicate the error estimation for H_0 . Thirdly, we can directly incorporate uncertainty in the galaxy peculiar velocity (V_p) into the uncertainty in H_0 through the prior on V_p .

In addition to the global parameters, each maser feature requires two parameters, its radius, r , and azimuth, ϕ , to specify its location in the disk. Initial values for r and ϕ for high-velocity features were estimated from the position data, assuming $\phi = 90^\circ$ for red-

shifted features and $\phi = -90^\circ$ for blue-shifted features. Systemic velocity features were assigned initial r values based on the acceleration data and ϕ values based on velocity data. All (r, ϕ) parameters were assigned flat priors and were adjusted in the fitting process.

We evaluated parameter *posteriori* PDFs with Markov chain Monte Carlo (MCMC) trials that were accepted or rejected according to the Metropolis-Hastings algorithm. All parameters except for one were given flat priors and hence could vary freely, constrained only by the difference between data and model. The only parameter with a constraining prior was the galaxy’s peculiar velocity, V_p ; this comes from large scale gravitational perturbations (Masters et al. 2006; Springob et al. 2007) which are expected to cause observed velocities for UGC 3789 to be lower by $151 \pm 163 \text{ km s}^{-1}$ with respect to the Hubble flow (i.e. $cz = V_0 + V_p$). All velocities quoted here are non-relativistic, optical definition, in the CMB frame; the model and the data velocities (shifted from the observed LSR frame to the CMB frame by adding 60 km s^{-1}) were converted internally in the fitting program to relativistically correct values. Initial runs indicated very little warping (as is evident in the VLBI images) and maser orbital eccentricities near zero. Hence, for our “basic model,” we used only the first order warping parameters and assumed circular gas orbits.

We ran 10 “burn-in” stages, each with 10^6 trials, in order to arrive at near optimum parameter values and parameter step sizes. Parameter step sizes were iteratively adjusted after each burn-in stage so as to come from Gaussian distributions with similar widths as the anticipated *posteriori* PDFs (estimated from the burn-in MCMC trials), multiplied by a global step-size factor. This factor (≈ 0.02) was also adjusted in the burn-in stages to scale parameter steps so that an optimal Metropolis-Hastings acceptance rate near 23% was achieved. The widths of the anticipated *posteriori* PDFs of the parameters and the global step-size factor, which together determine parameter step sizes, were taken from the last burn-in stage and then held constant for the final MCMC trials.

After discarding the burn-in stage trials, we evaluated 10^7 MCMC trials to obtain final *posteriori* PDFs. The Pearson product-moment correlation coefficients from these trials are given in Table 2. The only correlation coefficient (r) with magnitude greater than 0.5 is between the Hubble constant and central black hole mass ($r_{H_0, M} \approx -0.85$) (see discussion in Kuo et al. (2012)). In order to more optimally sample the PDFs for these parameters, we modified the MCMC values for these parameters to be totally anti-correlated for half of the trials and uncorrelated for the remainder (Gregory 2011).

From Bayes’ theorem, the probability density of the parameters (ρ), given a model (m), data (d), and priors (I), is given by

$$P(\rho|m, d, I) \propto P(d|\rho, m, I) \times P(\rho|m, I) \ .$$

Since we assume Gaussianly distributed uncertainties for the data and priors, maximizing $P(d|\rho, m, I) \times P(\rho|m, I)$ is equivalent to minimizing $\chi_d^2 + \chi_\rho^2$, where the subscripts d and ρ refer to the data and model parameters (given the priors), respectively. The best-fitting trial gave $\chi_d^2 = 1.50$ for 227 degrees of freedom. In Fig. 3, we show projections of the data with the best-fitting model superposed. The modeling also yields the (r, ϕ) coordinates of each maser feature in the disk plane, which are displayed in Fig. 4 (neglecting the slight warping of the disk).

Optimum values of the model parameters were estimated from the *posteriori* PDFs marginalized over all other parameters. They were generated from a total of 10^7 MCMC trials, obtained from 10 independent program runs starting with slightly different parameter values and new random number generator seeds. Each run produced 10^7 trials, but stored only every tenth trial (i.e. “thinned” by a factor of 10). Parameter values given in Table 3 were produced from binned histograms for each parameter and finding the sample median and $\pm 34\%$ ($\approx \pm 1\sigma$) range. Of some interest is the very accurate estimate of the mass of the central black hole of $(1.16 \pm 0.12) \times 10^7 M_\odot$.

The binned *posteriori* PDF for the Hubble constant, marginalized over all other parameters, is displayed in Fig. 5, and the marginalized distributions for the other 9 global parameters are shown in Fig. 6. The H_0 distribution can be well approximated by a Gaussian with a mean of $68.9 \text{ km s}^{-1} \text{ Mpc}^{-1}$ and a $\pm 34\%$ confidence range of $\sigma = \pm 5.8 \text{ km s}^{-1} \text{ Mpc}^{-1}$. Since, the reduced $\chi_\nu^2 = 1.50$, we conservatively inflate this uncertainty by a factor of $\sqrt{1.50}$ to $\pm 7.1 \text{ km s}^{-1} \text{ Mpc}^{-1}$. This Hubble constant, coupled with the recessional velocity of $cz = V_o + V_p = 3466 \text{ km s}^{-1}$ (optical definition relative to the CMB, and corrected for a peculiar velocity of 151 km s^{-1}), and assuming cosmological parameters for matter density $\Omega_m = 0.27$ and dark energy $\Omega_\Lambda = 0.73$, places UGC 3789 at an angular-diameter distance of $49.6 \pm 5.1 \text{ Mpc}$. This corresponds to a luminosity distance of $50.8 \pm 5.2 \text{ Mpc}$.

4.1. Sensitivity of H_0 to Data Weighting

We tested the sensitivity of our estimate of H_0 to significant ($> 30\%$) changes in the error floors applied to the data set of Table 1. Changing the positional error floors from 0.010 to 0.005 or 0.015 mas changed estimates of H_0 by less than $1 \text{ km s}^{-1} \text{ Mpc}^{-1}$. Varying the acceleration error floor from 0.57 to 0.27 or 0.87 $\text{km s}^{-1} \text{ yr}^{-1}$ produced similarly small changes in H_0 . Decreasing the velocity error floors for the systemic and high-velocity maser features from 1.0 and 0.3 km s^{-1} , respectively, to 0.7 and 0.2 km s^{-1} also yielded insignificant changes in H_0 .

In our tests, the only sensitivity of H_0 to changes in error floors occurred when increasing the velocity error floors for systemic and high-velocity maser features from 1.0 and 0.3 km s⁻¹, respectively, by 30% to 1.3 and 0.4 km s⁻¹. This resulted in estimates of H_0 reduced by 4 km s⁻¹ Mpc⁻¹. This small sensitivity likely comes from down-weighting the velocity information in the high-velocity masers. This information is critical to the method as it provides direct and strong constraints for the location (x_0, y_0) and velocity (V_0) of the central black hole. Down-weighting this data, by increasing its uncertainty, requires the program to use weaker, indirect information in the position/acceleration data to determine these parameters.

4.2. Secondary χ^2 Minima

In preliminary attempts to fit the data, we used a prior constraint for H_0 of 72 ± 12 km s⁻¹ Mpc⁻¹, probably at least double the current uncertainty in the Hubble constant. However, we ultimately dropped this constraint in favor of a flat prior on H_0 , allowing us to arrive at an estimate of H_0 from UGC 3789 data alone that is independent of prior knowledge. We then tested the sensitivity of the estimates of H_0 to the initial values. Starting with H_0 values as high as 80 km s⁻¹ Mpc⁻¹, we found fitted values returning close to our base result near 70 km s⁻¹ Mpc⁻¹. However, starting H_0 below 60 km s⁻¹ Mpc⁻¹, we found a stable fit with $H_0 = 59$ km s⁻¹ Mpc⁻¹.

The $H_0 = 59$ km s⁻¹ Mpc⁻¹ result likely comes from a secondary minimum in χ^2 space. For the fit returning $H_0 = 59$, $\chi^2 = 370.9$ for 227 degrees of freedom. This can be compared with the better $\chi^2 = 360.0$ (for the same 227 degrees of freedom) for our basic fit with $H_0 = 68.9$ km s⁻¹ Mpc⁻¹. Because the $H_0 = 59$ km s⁻¹ Mpc⁻¹ fit produces a significantly larger χ^2 , we exclude this trial.

4.3. Eccentric Gas Orbits

In order to assess the sensitivity of H_0 estimates to the assumption of circular gas orbits used in our basic model, we re-fit the data with a more general model with 3 additional parameters (e, ω and $\partial\omega/\partial r$) that allow eccentric gas orbits with pericentric angle changing linearly with radius in the accretion disk. Best-fit values for eccentricity were very small, 0.025 ± 0.008 , with pericenter at $-60^\circ \pm 20^\circ$ disk azimuth. Such a small eccentricity has a negligible effect on the other parameter estimates.

5. Dark Energy Constraints

Direct measurements of H_0 , such as from UGC 3789, are especially important for constraining the equation of state of dark energy, w , since the effects of dark energy are greatest at the present epoch. Our estimate of H_0 can be combined with results from the Wilkinson Microwave Anisotropy Probe (WMAP) mission to tighten constraints on the dark energy equation of state, w , *independent* of other methods such as using SN Ia or baryon acoustic oscillations (Eisenstein et al. 2005).

Fig. 7 shows 2-dimensional PDFs for w and H_0 with 95% and 68% confidence contours. The grey-scale contours were generated by binning the parameter values from Markov chains (`wmap_wcdm_sz_lens_wmap7.2_chains_norm_v4p1.tar.gz`) from the WMAP 7-year data (processed with WMAP version 4.1, RECFAST version 1.5 and modeled with a constant- w , Λ CDM model that incorporates the effects of the SZ effect and gravitational lensing). Fitting a Gaussian to the marginalized 1-dimensional PDF for w yields $w = -1.09 \pm 0.37$ ($\pm 68\%$ confidence).

Our new constraint that $H_0 = 68.9 \pm 7.1 \text{ km s}^{-1} \text{ Mpc}^{-1}$, when added to the WMAP PDF, is shown in Fig. 7 with dashed red contours. This information for H_0 , which is independent of w , improves the w -constraint by nearly a factor of two: $w = -0.98 \pm 0.20$. This is probably about as accurate a result as one can obtain from measurements of the water maser emission from UGC 3789 with current equipment and a reasonable amount of observing time. Significantly improved measurements of this galaxy will likely await the completion of the Square Kilometer Array’s high-frequency component.

Progress in the near future will come from measurements of other megamaser galaxies. The goal of the Megamaser Cosmology Project is to determine H_0 with $\pm 3\%$ accuracy via ≈ 10 megamaser galaxy measurements. For example, were such measurements to yield $H_0 = 68.9 \pm 2.1 \text{ km s}^{-1} \text{ Mpc}^{-1}$, this would further tighten the constraint on the equation of state of dark energy (blue dotted contours in Fig. 7) to $w = -0.97 \pm 0.10$, independent of other methods.

We are grateful to the NRAO VLBA and GBT staff for their many contributions to the Megamaser Cosmology Project. We thank the referee for many valuable comments on the original version of this paper.

Facilities: VLBA, GBT, Effelsberg

REFERENCES

- Argon, A. L., Greenhill, L. J., Reid, M. J., Moran, J. M. & Humphreys, E. M. L. 2007, *ApJ*, 659, 1040
- Braatz, J. A., Reid, M. J., Humphreys, E. M. L., et al. 2010, *ApJ*, 718, 657
- Bonamente, M., Joy, M. K., LaRoque, S. J., Carlstrom, J. E., Reese, E. D. & Dawson, K. S. 2006, *ApJ*, 647, 25
- Eisenstein, D. J., Zehavi, I., Hogg, D. W. et al. 2005, *ApJ*, 633, 560
- Freedman, W. et al. 2001, *ApJ*, 553, 47
- Gregory, P. C. 2011, *MNRAS*, 410, 94
- Herrnstein et al. 1999, *Nature*, 400, 539
- Hogg, D. W. 1999, arXiv:astro-ph/9905116v4
- Hu, W. 2005, in *ASP Conf. Ser. 339, Observing Dark Energy*, eds. S. C. Wolff & T. R. Lauer (San Francisco, CA: ASP), 215
- Humphreys, E. M. L., Reid, M. J., Greenhill, L. J., Moran, J. M. & Argon, A. L. 2008, *ApJ*, 672, 800
- Komatsu, E. Smith, K. M., Dunkley, J., et al. 2011, *ApJS*, 192, 18
- Kuo, C., Braatz, J. A., Reid, M. J. et al. arXiv:1207.7273
- Masters, K. L., Springob, C. M., Haynes, M. P., et al. 2006, *ApJ*, 653, 861
- Reid, M. J., Braatz, J. A., Condon, J. J., et al. 2009, *ApJ*, 695, 287
- Reid, B. A., Percival, W. J., Eisenstein, D. J. et al. 2010, *MNRAS*, 404, 60
- Riess, A. G., Macri, L., Casertano, S., et al. 2011, *ApJ*, 730, 119
- Sandage, A., Tammann, G. A., Saha, A., Reindl, B., Macchetto, F. D. & Panagia, N. 2006, *ApJ*, 653, 843
- Sivia, D. & Skilling, J. 2006, “Data Analysis: A Bayesian Tutorial, 2nd Edition,” (New York, Oxford Univ. Press Inc.), 168.
- Springob, C. M., Masters, K. L., Haynes, M. P. et al. 2007, *ApJS*, 172, 599

Suyu, S. H., Marshall, P. J., Auger, M. W., Hilbert, S., Blandford, R. D., Koopmans, L. V. E., Fassnacht, C. D. & Treu, T. et al. 2010, ApJ, 711, 201

Watson, W. D. & Wallin, B. K. 1994, ApJ, 432, L35

This preprint was prepared with the AAS L^AT_EX macros v5.2.

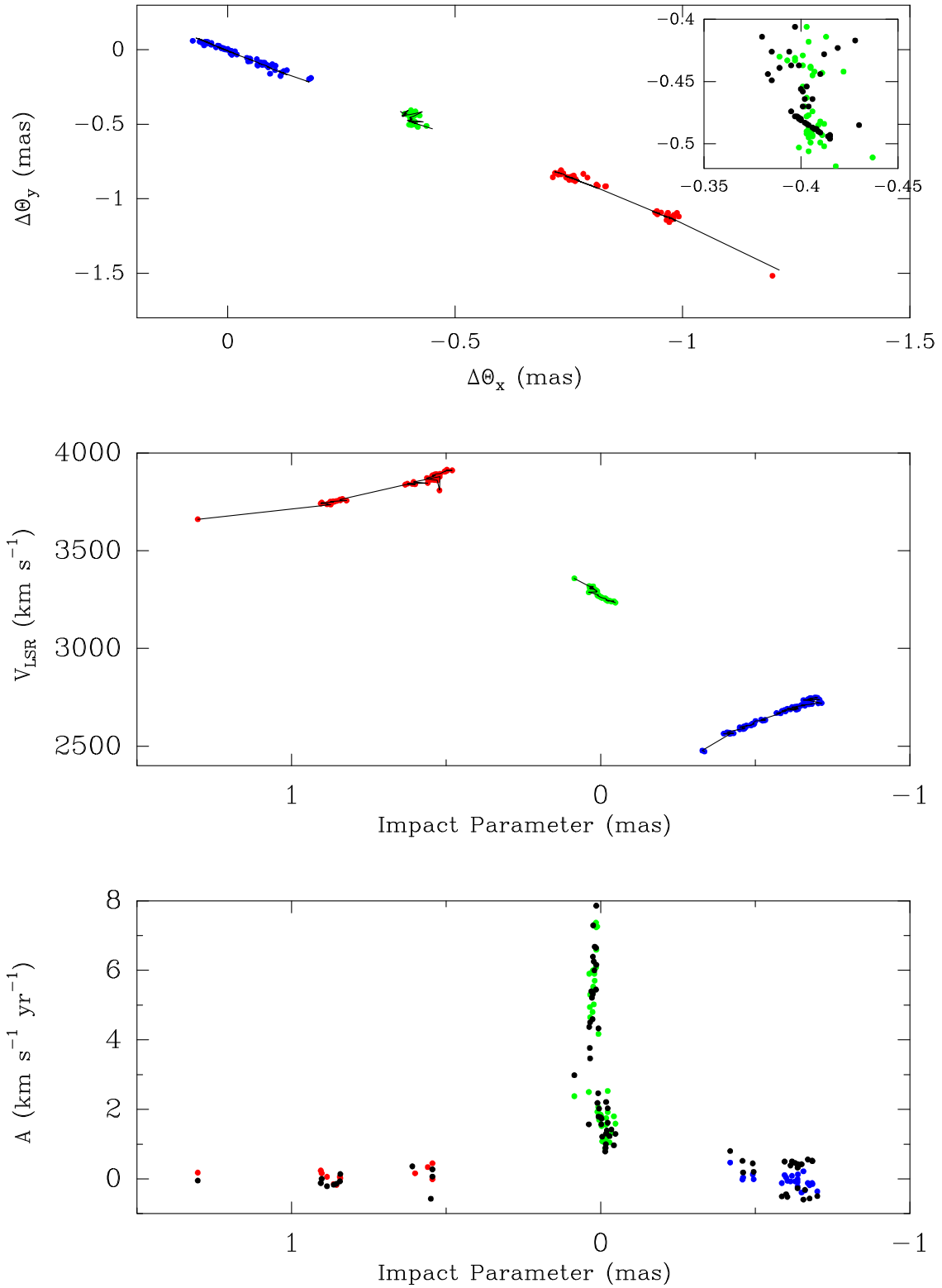


Fig. 3.— Data (colored dots) and best-fit model (lines and black dots). *Top panel:* Positions on the sky. Inset shows a blow-up of the systemic-velocity masers. *Middle panel:* LSR velocity versus position along the disk. *Bottom panel:* Accelerations versus impact parameter.

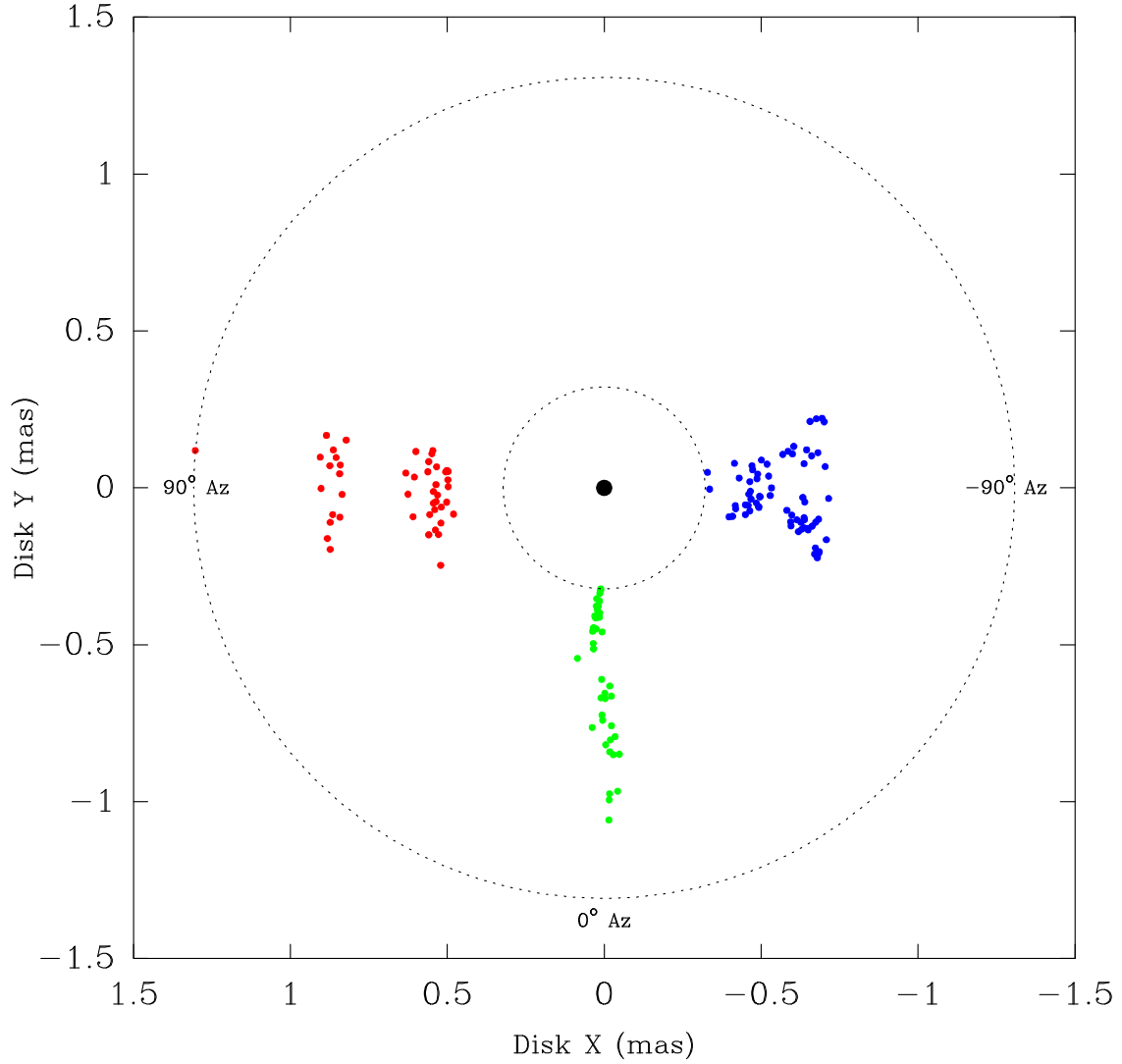


Fig. 4.— Location of maser features projected in the plane of the accretion disk based on the best-fit model. The location of the central black hole is shown with a *black filled circle* at the origin. The observer is at a large negative Y location. Disk azimuth defined is as 0° toward the observer. *Red and Blue* dots indicate the red-shifted (toward disk azimuth $\approx 90^\circ$) and blue-shifted (toward disk azimuth $\approx -90^\circ$) high-velocity masers, respectively. *Green* dots indicate the systemic velocity masers (toward disk azimuth $\approx 0^\circ$).

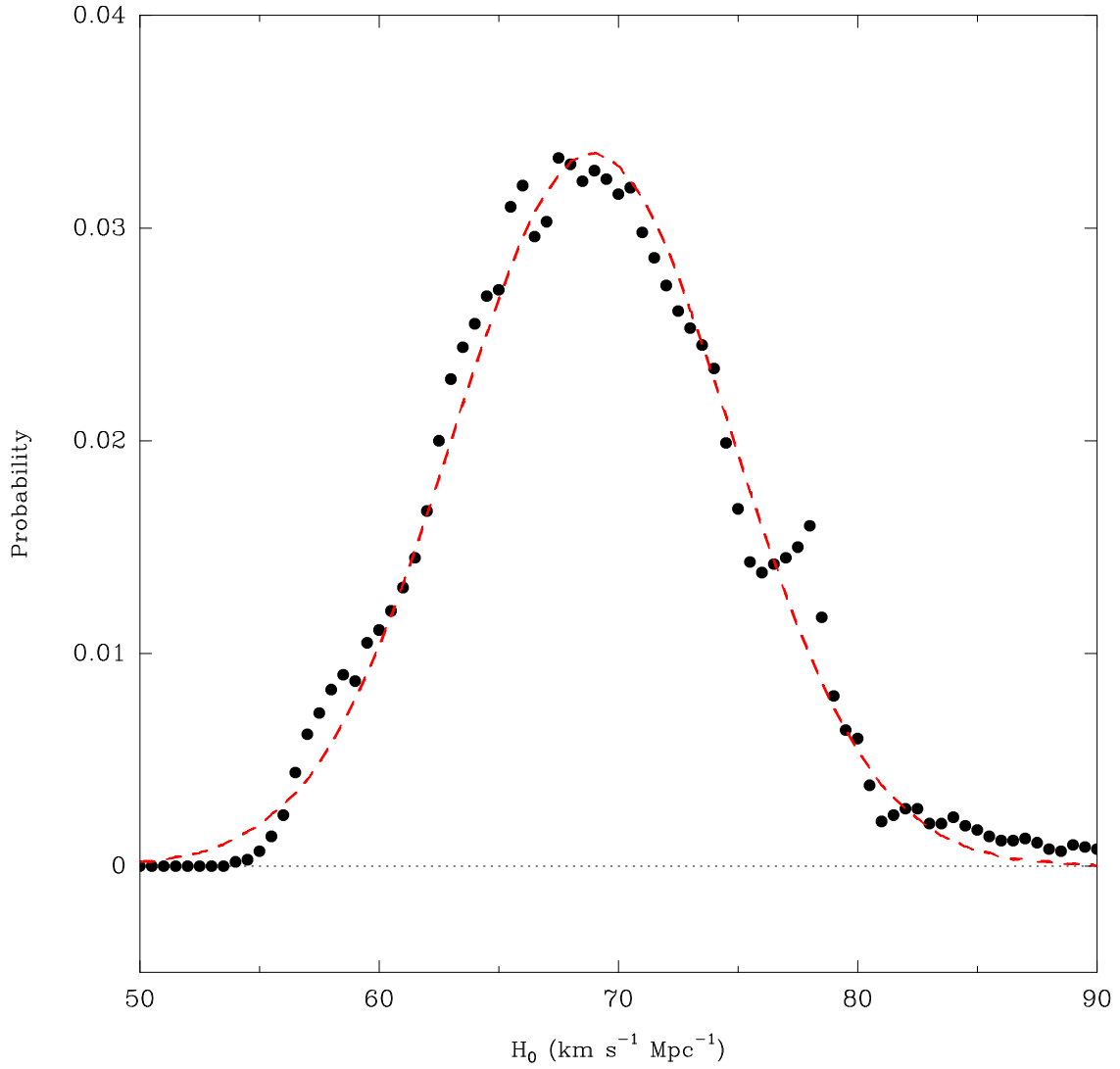


Fig. 5.— Posterior probability density function for the Hubble constant parameter (H_0), marginalized over all other parameters. Superposed (*dashed red line*) is a Gaussian with $\sigma = 5.8 \text{ km s}^{-1} \text{ Mpc}^{-1}$. Scaling the Gaussian width by $\sqrt{\chi^2_\nu}$ yields our estimate of the Hubble constant of $H_0 = 68.9 \pm 7.1 \text{ km s}^{-1} \text{ Mpc}^{-1}$.

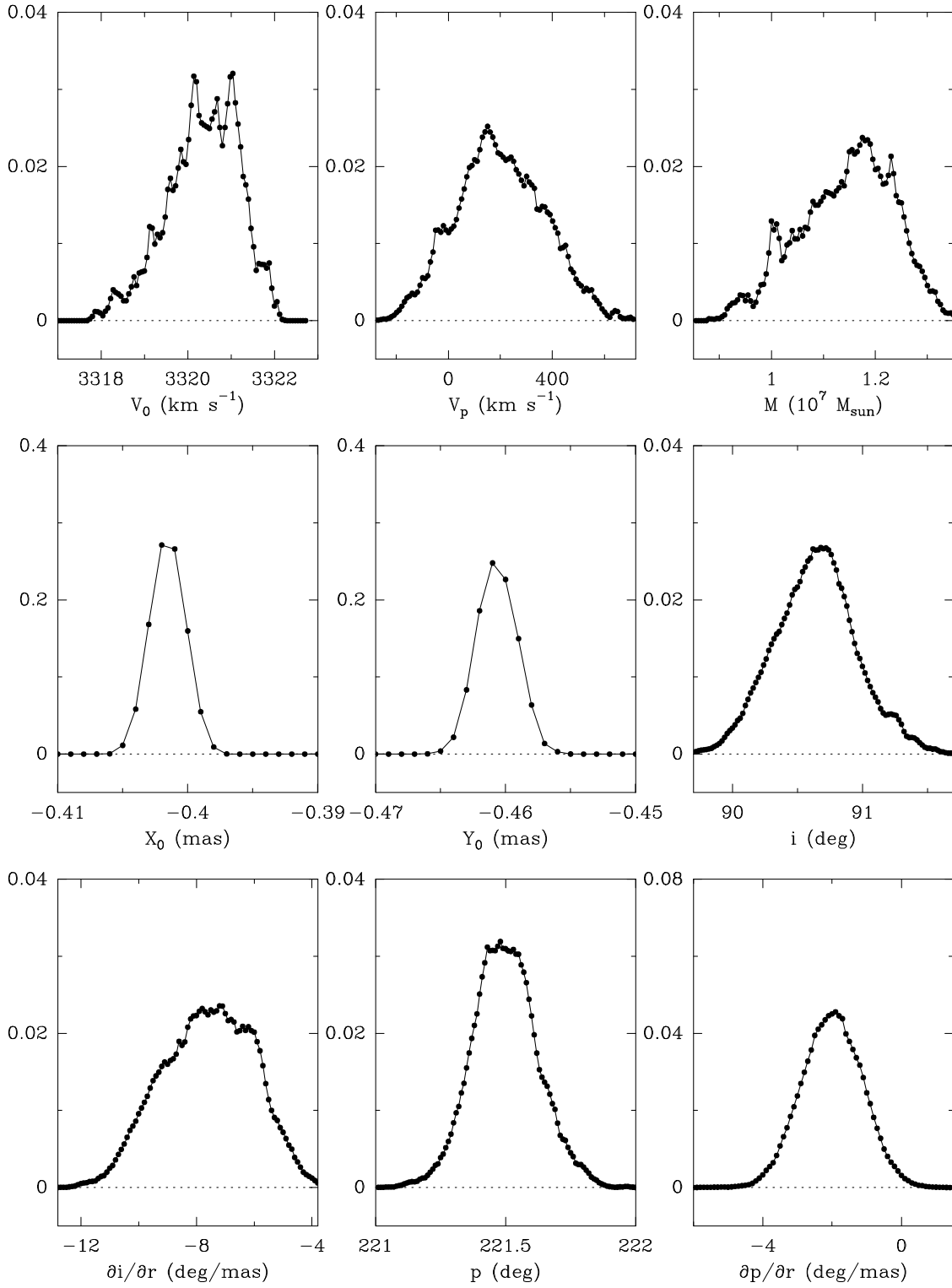


Fig. 6.— Marginalized posteriori probability density functions for the nine global parameters, excluding H_0 which is shown in Fig. 5.

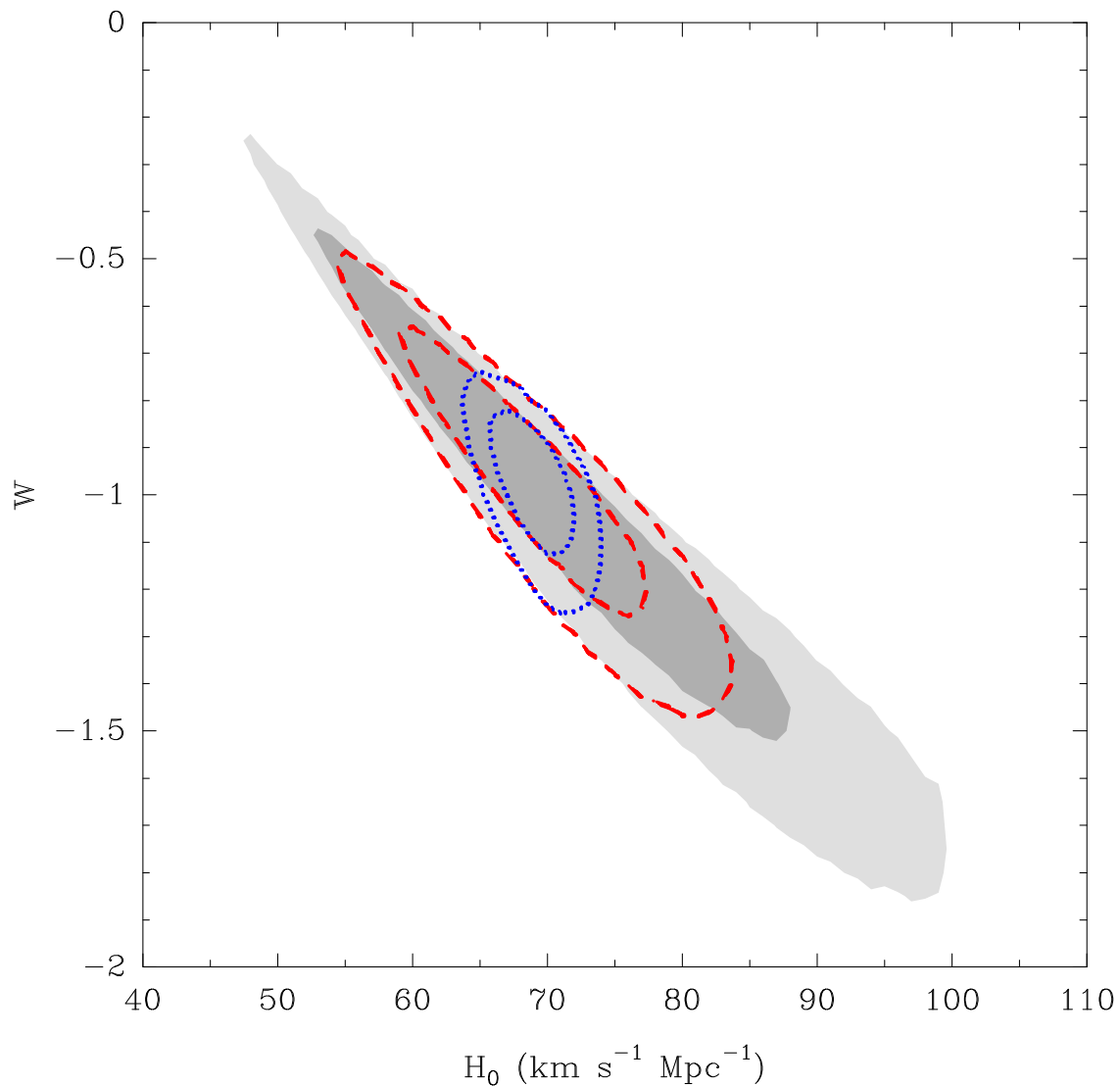


Fig. 7.— 2-D probability density functions for a (constant) equation of state of dark energy (w) and H_0 . *Grey scale contours* come from WMAP7.2 results. *Red dashed contours* combine the WMAP probability density function and the constraint that $H_0 = 68.9 \pm 7.1 \text{ km s}^{-1} \text{ Mpc}^{-1}$ from the results of UGC 3789 presented in this paper. *Blue dotted contours* anticipate an improved constraint of $H_0 = 68.9 \pm 2.1 \text{ km s}^{-1} \text{ Mpc}^{-1}$ from the results of ≈ 10 galaxies like UGC 3789, the goal of the Megamaser Cosmology Project. Contours enclose 68% and 95% probabilities.

Table 1. UGC 3789 H₂O Maser Data

V_{LSR} (km s ⁻¹)	Θ_x (mas)	σ_{Θ_x} (mas)	Θ_y (mas)	σ_{Θ_y} (mas)	A (km s ⁻¹ yr ⁻¹)	σ_A (km s ⁻¹ yr ⁻¹)
2472.8	-0.183	0.009	-0.190	0.009
2477.9	-0.179	0.008	-0.197	0.021
2562.9	-0.116	0.005	-0.176	0.028
2564.6	-0.119	0.004	-0.153	0.005
2566.3	-0.122	0.003	-0.149	0.003
2568.0	-0.123	0.003	-0.143	0.009	0.5	0.2
2569.7	-0.130	0.009	-0.137	0.007
2571.4	-0.093	0.020	-0.161	0.008
2586.7	-0.104	0.012	-0.137	0.012
2588.4	-0.089	0.004	-0.118	0.003	0.0	0.2
2590.1	-0.084	0.009	-0.102	0.005
2591.8	-0.087	0.008	-0.103	0.006
2593.5	-0.096	0.004	-0.107	0.004	0.0	0.2
2595.2	-0.098	0.004	-0.097	0.007
2596.9	-0.105	0.007	-0.107	0.015
2602.0	-0.066	0.010	-0.106	0.012
2603.7	-0.084	0.003	-0.102	0.009
2605.4	-0.076	0.007	-0.102	0.004
2607.1	-0.065	0.005	-0.102	0.004
2608.8	-0.067	0.015	-0.096	0.004
2610.5	-0.073	0.005	-0.089	0.007	0.0	0.2
2612.2	-0.077	0.003	-0.087	0.007	0.0	0.2
2613.9	-0.081	0.006	-0.087	0.007
2615.6	-0.068	0.007	-0.084	0.015	0.1	0.2
2617.3	-0.072	0.007	-0.085	0.007
2629.2	-0.045	0.012	-0.079	0.013
2630.9	-0.042	0.009	-0.054	0.010
2632.6	-0.049	0.004	-0.059	0.004
2634.3	-0.050	0.004	-0.077	0.004
2636.0	-0.064	0.008	-0.063	0.005
2668.3	-0.009	0.006	-0.034	0.007
2670.0	-0.020	0.006	-0.032	0.005
2678.5	-0.006	0.004	-0.024	0.004
2680.2	-0.016	0.003	-0.011	0.003	-0.1	0.2
2681.9	-0.008	0.002	-0.008	0.002
2683.6	-0.008	0.002	-0.008	0.002	0.0	0.2
2685.3	-0.005	0.002	-0.007	0.002	0.1	0.2

Table 1—Continued

V_{LSR} (km s^{-1})	Θ_x (mas)	σ_{Θ_x} (mas)	Θ_y (mas)	σ_{Θ_y} (mas)	A ($\text{km s}^{-1} \text{ yr}^{-1}$)	σ_A ($\text{km s}^{-1} \text{ yr}^{-1}$)
2687.0	0.000	0.002	0.000	0.002
2688.7	0.000	0.002	0.001	0.002	-0.1	0.2
2690.4	0.005	0.002	0.001	0.002
2692.1	0.000	0.003	0.005	0.002	-0.1	0.2
2693.8	0.009	0.002	0.006	0.002	0.0	0.2
2695.5	0.009	0.002	0.010	0.003
2697.2	0.010	0.003	0.007	0.004	-0.1	0.2
2698.9	0.014	0.002	0.010	0.002	0.1	0.2
2700.6	0.012	0.002	0.011	0.003	0.1	0.2
2702.3	0.011	0.002	0.011	0.003	-0.1	0.2
2704.0	0.013	0.003	0.011	0.004	-0.2	0.2
2705.7	0.019	0.003	0.026	0.003
2707.4	0.022	0.004	0.028	0.010	-0.3	0.2
2709.1	0.026	0.004	0.016	0.014
2710.8	0.036	0.007	0.033	0.007	-0.4	0.2
2712.5	0.052	0.004	0.029	0.007
2714.2	0.051	0.004	0.048	0.005
2715.9	0.036	0.014	0.046	0.005
2717.6	0.044	0.011	0.048	0.005
2719.3	0.062	0.006	0.054	0.009
2721.0	0.077	0.005	0.060	0.006	0.0	0.2
2734.6	0.046	0.003	0.045	0.005
2736.3	0.040	0.006	0.042	0.012	0.2	0.2
2738.0	0.045	0.008	0.054	0.006
2739.7	0.044	0.008	0.042	0.003	-0.1	0.2
2741.4	0.050	0.004	0.051	0.004	-0.1	0.2
2743.1	0.049	0.005	0.053	0.004	-0.1	0.2
2744.8	0.053	0.003	0.048	0.006	-0.2	0.2
2746.5	0.048	0.009	0.047	0.003
2748.2	0.058	0.004	0.050	0.005	-0.4	0.2
2749.9	0.058	0.004	0.052	0.014

Table 1—Continued

V_{LSR} (km s^{-1})	Θ_x (mas)	σ_{Θ_x} (mas)	Θ_y (mas)	σ_{Θ_y} (mas)	A ($\text{km s}^{-1} \text{ yr}^{-1}$)	σ_A ($\text{km s}^{-1} \text{ yr}^{-1}$)
3234.4	-0.403	0.010	-0.406	0.010	1.6	0.2
3239.5	-0.401	0.012	-0.429	0.005	1.3	0.2
3241.2	-0.404	0.005	-0.418	0.005	1.8	0.2
3242.9	-0.393	0.004	-0.433	0.004	2.5	0.2
3244.6	-0.389	0.003	-0.430	0.003	1.1	0.2
3246.3	-0.397	0.003	-0.433	0.004	1.9	0.2
3248.0	-0.397	0.004	-0.431	0.009	1.8	0.2
3249.7	-0.405	0.004	-0.438	0.008	1.6	0.2
3251.4	-0.405	0.003	-0.439	0.005	1.2	0.2
3253.1	-0.401	0.004	-0.437	0.005	1.0	0.2
3254.8	-0.413	0.007	-0.414	0.009	1.6	0.2
3256.5	-0.422	0.006	-0.442	0.011	0.9	0.2
3258.2	-0.411	0.004	-0.443	0.004	1.1	0.2
3259.9	-0.407	0.003	-0.442	0.008	1.5	0.2
3261.6	-0.406	0.004	-0.445	0.005	1.8	0.2
3263.3	-0.403	0.003	-0.463	0.015	1.9	0.2
3266.7	-0.401	0.009	-0.454	0.009	1.7	0.2
3268.4	-0.412	0.011	-0.484	0.007	1.9	0.2
3270.1	-0.402	0.006	-0.470	0.015	2.1	0.2
3271.8	-0.403	0.006	-0.478	0.006	1.9	0.2
3273.5	-0.404	0.006	-0.477	0.006	4.2	0.2
3287.1	-0.410	0.017	-0.482	0.008	2.5	0.8
3288.8	-0.406	0.004	-0.474	0.004	6.6	0.8
3290.5	-0.404	0.005	-0.506	0.005	6.1	0.8
3292.2	-0.409	0.003	-0.485	0.009	7.3	0.8
3293.9	-0.404	0.003	-0.487	0.003	8.4	0.8
3295.6	-0.403	0.003	-0.490	0.004	7.4	0.8
3297.3	-0.403	0.002	-0.492	0.006	7.2	0.8
3299.0	-0.405	0.002	-0.489	0.003	5.9	0.8
3300.7	-0.406	0.002	-0.489	0.004	5.7	0.8
3302.4	-0.409	0.002	-0.490	0.004	4.8	0.8
3304.1	-0.406	0.002	-0.493	0.002	4.7	0.8
3305.8	-0.404	0.002	-0.495	0.005	5.0	0.8
3307.5	-0.406	0.003	-0.494	0.005	5.4	0.8
3309.2	-0.404	0.002	-0.491	0.004	4.9	0.8
3310.9	-0.411	0.003	-0.493	0.003	5.9	0.8
3312.6	-0.410	0.003	-0.499	0.004	6.0	0.8
3314.3	-0.399	0.005	-0.503	0.005	5.3	0.8
3316.0	-0.412	0.010	-0.502	0.004	5.3	0.8
3317.7	-0.405	0.019	-0.499	0.005	5.5	0.8
3319.4	-0.418	0.015	-0.518	0.028	5.9	0.8
3358.5	-0.437	0.007	-0.511	0.006	2.4	0.2

Table 1—Continued

V_{LSR} (km s^{-1})	Θ_x (mas)	σ_{Θ_x} (mas)	Θ_y (mas)	σ_{Θ_y} (mas)	A ($\text{km s}^{-1} \text{ yr}^{-1}$)	σ_A ($\text{km s}^{-1} \text{ yr}^{-1}$)
3660.7	-1.198	0.010	-1.517	0.012	0.2	0.2
3735.5	-0.977	0.005	-1.139	0.008
3737.2	-0.980	0.006	-1.133	0.004	0.1	0.2
3738.9	-0.992	0.012	-1.119	0.011
3740.6	-0.971	0.005	-1.157	0.005	0.2	0.2
3745.7	-0.965	0.014	-1.143	0.020	0.2	0.2
3747.4	-0.973	0.006	-1.123	0.009
3749.1	-0.981	0.009	-1.109	0.005	-0.1	0.2
3750.8	-0.988	0.007	-1.095	0.007
3752.5	-0.965	0.011	-1.111	0.005
3754.2	-0.968	0.015	-1.094	0.008	-0.2	0.2
3755.9	-0.940	0.008	-1.092	0.004
3757.6	-0.953	0.006	-1.092	0.005	0.0	0.2
3759.3	-0.945	0.003	-1.104	0.004
3761.0	-0.944	0.004	-1.101	0.004	0.1	0.2
3764.4	-0.944	0.014	-1.082	0.015
3808.6	-0.782	0.006	-0.833	0.006
3837.5	-0.830	0.010	-0.917	0.028
3839.2	-0.811	0.009	-0.905	0.011	0.2	0.2
3840.9	-0.814	0.010	-0.914	0.005
3842.6	-0.832	0.006	-0.916	0.007
3846.0	-0.766	0.012	-0.874	0.014
3851.1	-0.791	0.007	-0.858	0.029
3859.6	-0.760	0.004	-0.848	0.005
3861.3	-0.764	0.004	-0.866	0.004
3863.0	-0.764	0.004	-0.882	0.004
3864.7	-0.760	0.007	-0.874	0.005
3866.4	-0.761	0.009	-0.868	0.007	0.3	0.2
3868.1	-0.765	0.010	-0.870	0.004
3871.5	-0.751	0.030	-0.874	0.021
3878.3	-0.761	0.016	-0.845	0.023
3880.0	-0.758	0.004	-0.871	0.004
3881.7	-0.750	0.004	-0.863	0.003	0.5	0.2
3883.4	-0.753	0.003	-0.854	0.009
3885.1	-0.746	0.003	-0.854	0.013	0.0	0.2
3886.8	-0.750	0.007	-0.865	0.005
3890.2	-0.758	0.024	-0.849	0.017
3891.9	-0.744	0.008	-0.857	0.007
3893.6	-0.715	0.006	-0.856	0.007
3903.8	-0.738	0.007	-0.830	0.005
3905.5	-0.727	0.005	-0.838	0.011
3907.2	-0.733	0.004	-0.835	0.008
3908.9	-0.727	0.004	-0.833	0.009
3910.6	-0.720	0.003	-0.827	0.004
3912.3	-0.730	0.007	-0.824	0.007
3914.0	-0.733	0.006	-0.809	0.014

Table 2. Parameter Correlation Coefficients

	H_0	M	V_0	x_0	y_0	i	$\partial i/\partial r$	p	$\partial p/\partial r$	V_p
H_0	1.000	-0.846	0.024	0.029	0.061	0.318	0.084	0.034	-0.027	0.410
M	-0.846	1.000	0.024	-0.021	-0.071	-0.432	-0.157	-0.019	0.027	0.128
V_0	0.024	0.024	1.000	-0.011	0.053	-0.018	-0.254	0.314	-0.003	0.073
x_0	0.029	-0.021	-0.011	1.000	0.162	-0.371	0.029	-0.217	0.215	0.023
y_0	0.061	-0.071	0.053	0.162	1.000	0.193	-0.337	0.183	-0.268	-0.013
i	0.318	-0.432	-0.018	-0.371	0.193	1.000	0.016	0.213	-0.196	-0.153
$\partial i/\partial r$	0.084	-0.157	-0.254	0.029	-0.337	0.016	1.000	-0.086	0.179	-0.112
p	0.034	-0.019	0.314	-0.217	0.183	0.213	-0.086	1.000	-0.433	0.023
$\partial p/\partial r$	-0.027	0.027	-0.003	0.215	-0.268	-0.196	0.179	-0.433	1.000	-0.007
V_p	0.410	0.128	0.073	0.023	-0.013	-0.153	-0.112	0.023	-0.007	1.000

Note. — Pearson product-moment correlation coefficients calculated from 10^7 McMC trial parameter values. Parameter definitions are given in the text and the notes in Table 3

Table 3. UGC 3789 Basic Disk Model

Parameter	Priors	Posterioris	Units
H_0	...	68.9 ± 7.1	$\text{km s}^{-1} \text{Mpc}^{-1}$
V_0	...	3320 ± 1	km s^{-1}
V_p	151 ± 163	146 ± 175	km s^{-1}
M	...	1.16 ± 0.12	$10^7 M_\odot$
x_0	...	-0.402 ± 0.002	mas
y_0	...	-0.460 ± 0.002	mas
$i(r_{ref})$...	90.6 ± 0.4	deg
$\partial i / \partial r$...	-7.6 ± 2.0	deg mas^{-1}
$p(r_{ref})$...	221.5 ± 0.2	deg
$\partial p / \partial r$...	-2.0 ± 1.1	deg mas^{-1}
e	0	0	...
ω	0	0	deg
$\partial \omega / \partial r$	0	0	deg mas^{-1}

Note. — Parameters are as follows: Hubble constant (H_0), observed velocity of the central black hole V_0 (non-relativistic, optical definition in CMB frame), peculiar velocity V_p with respect to Hubble flow in cosmic microwave background frame (i.e. $cz = V_0 + V_p$), black hole mass (M), eastward (x_0) and northward (y_0) position of black hole with respect to the reference masers ($2684 < V_{LSR} < 2693 \text{ km s}^{-1}$), disk inclination $i(r_{ref})$ at the reference angular radius of 0.60 mas, and inclination warping (change of inclination with radius: $\partial i / \partial r$), disk position angle $p(r_{ref})$ at the reference angular radius and position angle warping (change of position position angle with radius: $\partial p / \partial r$), gas orbital eccentricity (e) and angle of pericenter with respect to the line of sight (ω) and its derivative with angular radius ($\partial \omega / \partial r$). Flat priors were used, except where listed. Posteriori values are medians of their marginalized probability density functions and uncertainties give $\pm 34\%$ confidence ranges, scaled by the square-root of the (reduced) chi-squared per degree of freedom (except for V_p which is controlled by its prior).